

Article

Evaluation of the Surface Water Distribution in North-Central Namibia Based on MODIS and AMSR Series

Hiroki Mizuochi ^{1,*}, Tetsuya Hiyama ², Takeshi Ohta ³ and Kenlo N. Nasahara ⁴

¹ Graduate School of Life and Environmental Sciences, University of Tsukuba, 1-1-1 Tennodai, Tsukuba, Ibaraki 305-8572, Japan

² Hydrospheric Atmospheric Research Center (HyARC), Nagoya University, Furo-cho, Chikusa-ku, Nagoya 464-8601, Japan; E-Mail: hiyama@hyarc.nagoya-u.ac.jp

³ Graduate School of Bioagricultural Sciences, Nagoya University, Furo-cho, Chikusa-ku, Nagoya 464-8601, Japan; E-Mail: takeshi@agr.nagoya-u.ac.jp

⁴ Faculty of Life and Environmental Sciences, University of Tsukuba, 1-1-1 Tennoudai, Tsukuba, Ibaraki 305-8572, Japan; E-Mail: 24dakenlo@gmail.com

* Author to whom correspondence should be addressed; E-Mail: hiroki.mizuochi@gmail.com; Tel./Fax: +81-29-853-4897.

Received: 31 March 2014; in revised form: 5 August 2014 / Accepted: 6 August 2014 /

Published: 19 August 2014

Abstract: Semi-arid North-central Namibia has high potential for rice cultivation because large seasonal wetlands (*oshana*) form during the rainy season. Evaluating the distribution of surface water would reveal the area potentially suitable for rice cultivation. In this study, we detected the distribution of surface water with high spatial and temporal resolution by using two types of complementary satellite data: MODIS (MODerate-resolution Imaging Spectroradiometer) and AMSR-E (Advanced Microwave Scanning Radiometer–Earth Observing System), using AMSR2 after AMSR-E became unavailable. We combined the modified normalized-difference water index (MNDWI) from the MODIS data with the normalized-difference polarization index (NDPI) from the AMSR-E and AMSR2 data to determine the area of surface water. We developed a simple gap-filling method (“database unmixing”) with the two indices, thereby providing daily 500-m-resolution MNDWI maps of north-central Namibia regardless of whether the sky was clear. Moreover, through receiver-operator characteristics (ROC) analysis, we determined the threshold MNDWI (−0.316) for wetlands. Using ROC analysis, MNDWI had moderate performance (the area under the ROC curve was 0.747), and the recognition error for seasonal wetlands and dry land was 21.2%. The threshold MNDWI let us calculate probability of water presence

(PWP) maps for the rainy season and the whole year. The PWP maps revealed the total area potentially suitable for rice cultivation: 1255 km² (1.6% of the study area).

Keywords: surface water distribution; MODIS; AMSR-E; AMSR2; database unmixing; ROC analysis

1. Introduction

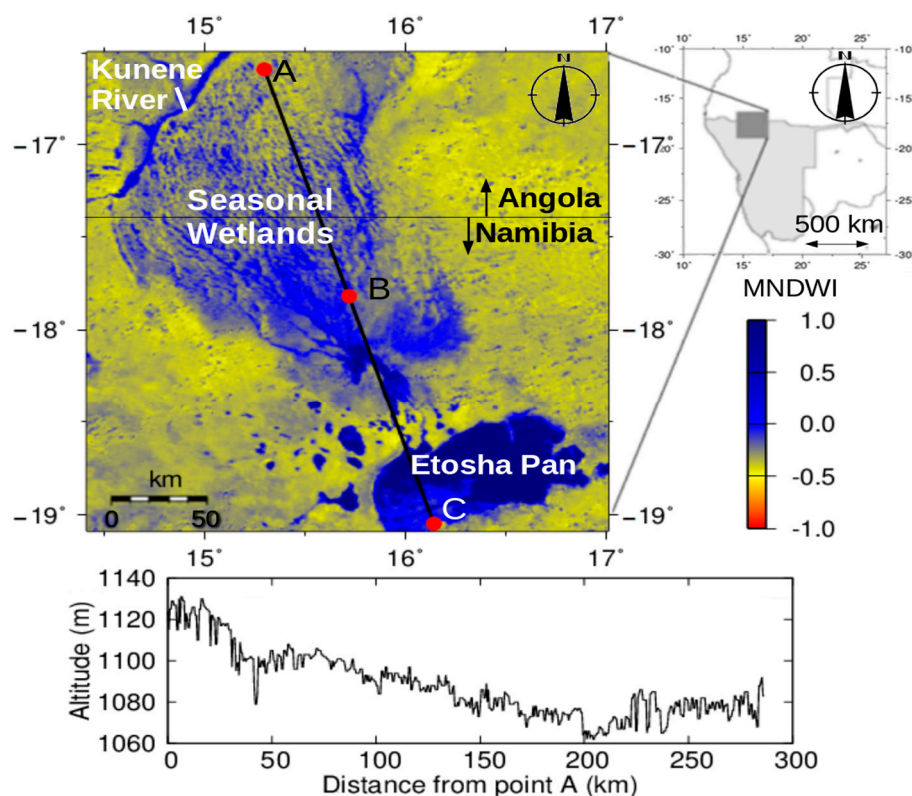
In North-central Namibia, where a quarter of Namibia's population lives, there is a significant risk of poor harvests because of the region's unstable rainfall [1]. In this area, the annual precipitation ranges from 50 to 600 mm between years [2]. On this basis, it is classified as a semi-arid region, but that is potentially misleading because the precipitation variation can produce drought or flooding in the same part of the country in different years. This unstable water supply makes farming difficult because farmers mainly cultivate pearl millet (*Pennisetum glaucum*) [3], which is somewhat drought-tolerant, but is severely damaged by this region's extreme fluctuations in water availability.

During the rainy season, vast wetlands (locally called *oshana*) form, often causing flooding. *Oshana* resemble shallow and widespread ephemeral rivers, with enormous channels. The water in *oshana* appears only during the rainy season, forming a vast wetland network. The extent of water in the *oshana* changes dynamically, even during a few days, in response to the unstable precipitation (Figure 1). The region where these seasonal wetlands appear is called Cuvelai, and the network of seasonal wetlands is called the Cuvelai System Seasonal Wetlands (CSSW). The northern edge of the CSSW is on the Angolan Plateau, and the southern edge forms the Etosha Pan, the biggest salty pan in Africa (Figure 2). Flood water comes from the Angolan Plateau during the rainy season, filling the *oshana* and eventually flowing towards the Etosha Pan. Some of the water mixes with rain, evaporates into the air, or infiltrates into the ground [4].

Figure 1. An example of the dramatic changes in the water extent in the *oshana* over the period of a week. These photos were taken from a water tower at the University of Namibia (15°17'44"E, 17°40'45"S) using a time-lapse digital camera (GardenWatchCam, Brinno Inc., Walnut, CA, USA).



Figure 2. (Top) The study region and (bottom) the altitude profile along the transect from the Angolan Plateau shown in the map. The transect was drawn along the seasonal river drainage pathway. The profile was created from global 30-arc-second elevation (GTOPO30) data [5]. On this basis, we calculated the average bed slope. Three test sites, distributed at equal distances along the transect, were used to determine the correlation between the modified normalized-difference water index (MNDWI) and the normalized-difference polarization index (NDPI): A ($15^{\circ}17'59''\text{E}$, $16^{\circ}35'23''\text{S}$) represents the Angolan Plateau, B ($15^{\circ}43'20''\text{E}$, $17^{\circ}49'09''\text{S}$) represents the center of the seasonal wetlands, and C ($16^{\circ}08'40''\text{E}$, $19^{\circ}02'54''\text{S}$) represents the Etosha Pan. The background image is the MNDWI distribution derived from MODIS data (24 March 2008).



Researchers have looked for ways to make farming more robust in this region despite the unstable water supply, e.g., [6,7]. The results suggested that a combination of pearl millet farming with rice (*Oryza* spp.) cultivation is a promising solution: the pearl millet is more tolerant of drought, whereas the rice is more tolerant of flooding. To minimize the risk of crop failure and, thereby, mitigate the region's food insecurity, there have been many government attempts to introduce rice cultivation to northern Namibia, but unfortunately these trials failed, without producing scientific data that could be used to identify the source of the failures [8]. To provide such a scientific assessment and to determine whether it would be possible to introduce rice cultivation sustainably, a Japanese government research program, the Science and Technology Research Partnership for Sustainable Development (SATREPS), is now underway, in partnership with the University of Namibia [9]. As pearl millet is indigenous to the region, the local farmers understand its requirements well. However, the cultivation of rice is new for them. Thus, before rice cultivation can be adopted in this region, research is required to understand its characteristics and its feasibility from various perspectives. Some researchers have pointed out that

the ephemeral wetlands in Cuvelai have high potential for rice production, e.g., [8–10]. However, there are no maps that define the area that would be potentially suitable for rice cultivation. In the present study, our goal was to estimate this area from the perspective of water supply (*i.e.*, the area that retains enough water for long enough during the rainy season to grow rice). To achieve this goal, we developed a new method based on satellite remote sensing to provide such maps, and then used a new method to evaluate the distribution of surface water in the CSSW, thereby revealing the area potentially suitable for rice cultivation. Some of this area may be unsuitable for rice cultivation for other reasons (e.g., political factors), but this analysis provides a good starting point for additional analysis.

To accurately estimate the distribution of the surface water, maps with high spatial and temporal resolution are required. MODIS (the MODerate-resolution Imaging Spectroradiometer) is a promising sensor for frequent monitoring over large areas, but, in practice, its temporal resolution may be low because clouds interfere with data collection, especially during the rainy season. In fact, the MODIS data in this region during the rainy season covers only 53% of pixels, on average (*i.e.*, we only can obtain data approximately every two days for a given pixel), even if we use MODIS products derived from both Terra and Aqua. This rate decreases further with increasing cloud cover, to 36% (approximately every three days) in the middle of the rainy season (January). Such temporally sparse data would not be sufficient to let researchers track the dynamic changes in the extent of water in detail during the period of a few days. Since the cloud cover increases during the most hydrologically important period, a weather-independent remote-sensing tool must be developed. A useful alternative is the AMSR (Advanced Microwave Scanning Radiometer) series, especially the AMSR-E and AMSR2 products. These passive microwave sensors can see through clouds (*i.e.*, they are weather-independent), but unfortunately, they have too-low spatial resolution to detect the scale of wetlands: the width of the *oshana* ranges from 200 m to 2 km [11], but the spatial resolution of the AMSR series is at least several kilometers. Thus, relying solely on MODIS or AMSR data cannot provide a solution. However, by combining the MODIS and AMSR series, it may be possible to achieve suitable spatial and temporal coverage to allow monitoring of surface water, which would allow creation of maps of the area potentially suitable for rice cultivation.

Other researchers have looked for various ways to combine MODIS and AMSR series. However, it is not yet clear how best to combine data from the two types of sensors. For example, Takeuchi and Gonzalez [12] and Zheng *et al.* [13] used linear regression models, whereas Dasgupta and Qu [14] used a wavelet technique. Unfortunately, linear regression could not describe the spatial pattern of the water distribution, whereas the wavelet technique did not provide sufficient accuracy. In this paper, we propose a simple and direct alternative, which we call “database unmixing”. In this approach, we first calculate two daily water indices (which we will define in Section 2.3): the modified normalized-difference water index (MNDWI) from the MODIS data and the normalized-difference polarization index (NDPI, [12,13]) from the AMSR-E and AMSR2 data. Although Zheng *et al.* called NDPI the polarization ratio index (PRI) [13], we have not used that abbreviation in order to avoid confusion with the “photochemical reflectance index” [15]. After calculation of the two water indices, we applied gap-filling to the original cloud-contaminated pixels in the MODIS MNDWI maps by using database unmixing. The basic concept is that we infer the spatial pattern of the MODIS MNDWI values from the AMSR-E and AMSR2 NDPI by matching past MNDWI maps with NDPI maps that are used as a training dataset. Specifically, we replaced each original cloud-contaminated MODIS pixel with a past

cloud-free MODIS pixel at which the corresponding AMSR-E/AMSR2 NDPI value was approximately the same as the original pixel's NDPI. Our results suggest that database unmixing successfully reproduced the spatial pattern of MNDWI from NDPI throughout the study area.

2. Materials and Methods

2.1. Study Site

Our study site covers the entire CSSW area using a 10×10 grid of AMSR-E/AMSR2 pixels, stretching from $16^{\circ}29'43''\text{S}$ to $19^{\circ}05'20''\text{S}$ and from $14^{\circ}24'59''\text{E}$ to $17^{\circ}00'53''\text{E}$. Each AMSR-E/AMSR2 pixel is $25 \text{ km} \times 25 \text{ km}$. Most of the wetlands in north-central Namibia appear in this region during the rainy season (from November to April) and disappear during the dry season (from May to October), except for artificial ponds, the Kunene River, and part of the Etosha Pan. Figure 2 illustrates the study area superimposed on a map of MNDWI during the rainy season. There are three areas where water is likely to exist during the rainy season: in the Kunene River at the northwestern edge of the study area, in seasonal wetlands (the *oshana* network) in the center, and in the Etosha Pan at the southeastern edge of the study area. The rest of the area mainly comprises savannas with arenosols [4], which are not suitable for agriculture.

The CSSW has extremely flat topography: from the southern edge of Angola to the northern edge of the Etosha Pan, the average bed slope is 1/3300. This is why the seasonal flooding spreads over such a wide area.

2.2. Preprocessing of MODIS and AMSR-E/AMSR2 Data

Table 1 summarizes the characteristics of the data utilized in this study. We downloaded MODIS daily products for the atmospherically corrected surface reflectance (MOD09GA and MYD09GA; scene IDs h19v10, h19v11, and h20v10) from the National Aeronautics and Space Administration (NASA) Land Processes Distributed Active Archive Center (LP DAAC) for the period from 2002 to 2013 [16]. MOD09GA is derived from the Terra satellite, and MYD09GA is derived from the Aqua satellite. We downloaded AMSR-E daily products for the atmospherically corrected global brightness temperature (Level 3) from the NASA DAAC at the National Snow and Ice Data Center (NSIDC) [17]. Unfortunately, AMSR-E, which is aboard Aqua, ceased operation in 2011, so the data were only available from 2002 to 2011. For 2012 and 2013, we used global brightness-temperature products derived from AMSR2 on the Global Change Observation Mission 1st-Water (GCOM-W1) satellite, which are available from the Japan Aerospace Exploration Agency (JAXA) GCOM-W1 site [18].

For the MODIS processing, we used the MODIS Reprojection Tool provided by LP DAAC. From the MOD09GA and MYD09GA products, we chose bands 1, 3, 4, and 7 to calculate MNDWI, as well as the quality control (QC) flag and the state flag for screening out unsuitable data, at 500-m spatial resolution. Bands 1, 3, 4, and 7 represent the reflectance at red, blue, green, and shortwave infrared (SWIR) wavelengths, respectively, which are required to calculate MNDWI. Although SWIR from the products could potentially be replaced by band 6, the MODIS band 6 detectors failed on Aqua shortly after its launch [19], thus, band 7 was the only available choice. We combined the three tiles that covered the study area into a single map for each day during our study period, with the values

converted from the original integrated sinusoidal projection into the latitude-longitude coordinate system of the World Geodetic System WGS84 datum. Resampling used the nearest-neighbor protocol. We then imported the resampled maps into the Geographic Resources Analysis Support System (GRASS) [20], and screened out any pixels for which the sensor reported problems or contamination by clouds or cloud shadows by checking the QC and state flags, with a 3 km buffer. That is, we screened out low-quality cloud-contaminated or cloud-shadow-contaminated pixels from the original maps, and also removed pixels within 3 km from these screened pixels. This distance setting for the buffer was based on empirical optimization: when we tried a smaller buffer distance, many clouds and cloud shadows survived the screening process, whereas a larger buffer distance decreased the original MODIS data available for subsequent analysis.

Table 1. Characteristics of the satellite data utilized in this study. SWIR, short-wave infrared.

Characteristic	MODIS	AMSR-E, AMSR2
Product	MOD09GA, MYD09GA	Level 3
Dates	MOD09GA: 1 January 2002 to 31 December 2013 MYD09GA: 4 July 2002 to 31 December 2013	AMSR-E: 19 June 2002 to 3 October 2011 AMSR2: 2 July 2012 to 31 December 2013
Spatial resolution	500 m	25 km
Bands used	B1 (red), B3 (blue), B4 (green), B7 (SWIR)	36.5 GHz (horizontal and vertical polarizations)
Index	MNDWI	NDPI

For the AMSR-E and AMSR2 processing, we used the HDF-EOS to GeoTIFF conversion tool provided by DAAC at NSIDC. Although AMSR-E and AMSR2 have 7 frequency bands in two polarizations, we chose the 36.5 GHz frequency to calculate NDPI, and included both the vertically and the horizontally polarized data. The 36.5 GHz channel is the optimal choice because it is less affected by the atmosphere than the highest AMSR-E frequency (89 GHz), and its spatial resolution is higher than that of the lower frequency channels (from 6.925 to 23.8 GHz) [13]. We used data from both ascending and descending orbits. We converted these data from the original equal-area scalable Earth projection into the WGS84 latitude-longitude coordinate system using nearest-neighbor resampling, and imported the data into GRASS. For the AMSR2 product, we could acquire higher spatial resolution for the AMSR2 maps (10 km) than for the AMSR-E maps (25 km), but we chose the lower resolution (25 km) of AMSR2 maps to simplify the algorithm.

2.3. Calculation of the Two Water Indices

For optical sensors such as MODIS, the normalized-difference water index (NDWI) has often been used to detect surface water:

$$NDWI = \frac{R - SWIR}{R + SWIR} \quad (1)$$

where R is the reflectance in the red band (wavelengths of 620 to 670 nm, corresponding to MODIS band 1), and $SWIR$ is the reflectance in the short-wave infrared band (wavelengths of 2105 to 2155 nm,

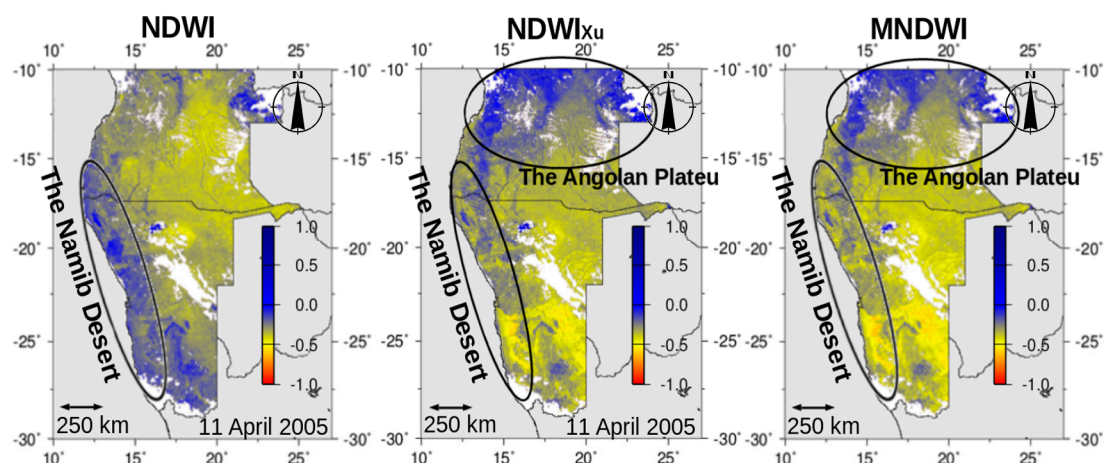
corresponding to MODIS band 7). This form of NDWI was defined by Takeuchi and Yasuoka [21], and differs from other similar indicators called NDWI [22–24]. NDWI is sensitive to surface water because in water-covered areas or mixed cells that contain both dry land and wetlands, the reflectance of SWIR becomes very low compared with that of visible bands, such as red [25].

To apply NDWI in our research, it was necessary to compensate for a significant disadvantage created by the color of the ground. In this region, red soil is ubiquitous, and NDWI would be biased by the high reflectance of this red color. To account for this bias, we first tried using the green band instead of red as the visible band. This NDWI is the same as that of Xu [23]:

$$NDWI_{Xu} = \frac{G - SWIR}{G + SWIR} \quad (2)$$

where G is reflectance in the green band (wavelengths of 545 to 565 nm, which corresponds to MODIS band 4), and we expressed this as $NDWI_{Xu}$. We confirmed that $NDWI_{Xu}$ mitigated the effects of the red soils (Figure 3). The Namib Desert, which lies on the western coast of Namibia and contains large areas of red sand, revealed implausibly high values for NDWI, which were not present in the $NDWI_{Xu}$ map.

Figure 3. Comparison among (Left) Takeuchi’s NDWI value based on data from the red and SWIR bands, (Center) Xu’s $NDWI_{Xu}$ value based on data from the green and SWIR bands, and (Right) MNDWI from the present study based on the MODIS data from the red, green, blue, and SWIR bands. NDWI is biased by the widespread red soils that occur in the study area (particularly in the Namib Desert), whereas $NDWI_{Xu}$ is biased by the abundance of green vegetation (particularly in the Angolan Plateau); MNDWI corrects for these problems. The white areas represent pixels eliminated from the map due to cloud contamination.



However, the Angolan Plateau showed too-high values of $NDWI_{Xu}$. We confirmed the presence of a widespread green background for the plateau due to the high vegetation cover by using Google Earth and Panoramio [26] for the area between 20°28'18"E and 20°22'08"E and between 11°55'52"S and 09°01'29"S. This type of background bias also potentially occurs within the study area in Namibia. Thus, additional modification was required to ensure robustness of the water index despite the two forms of color bias. Given the theoretical basis for NDWI, which relies on detecting differences between visible bands and the SWIR band, we modified NDWI to use the average of the three visible

colors instead of using only the red or green bands. On this basis, we developed a modified NDWI (*i.e.*, MNDWI):

$$\text{MNDWI} = \frac{R + G + B - 3 \text{ SWIR}}{R + G + B + 3 \text{ SWIR}} \quad (2)$$

where B is the reflectance in the blue band (wavelengths of 459 to 479 nm, which corresponds to MODIS band 3). MNDWI ranges from -1 to 1 , and like NDWI, it reaches its maximum value in water-covered areas. In our study area, MNDWI usually ranged from -0.5 to -0.3 in dry areas, and increased to near 0 in water-covered areas. Positive values were sometimes observed in deeply flooded areas. We confirmed that incorporating two additional visible bands in our calculation mitigated the effects of red soils compared to NDWI, and somewhat mitigated the effects of green vegetation compared to NDWI_{Xu} (Figure 3). Thus, we used MNDWI as the better index to avoid the bias caused by background colors in the visible spectrum.

From the MODIS data from both Terra and Aqua, we calculated MNDWI and calibrated the Terra MNDWI against the Aqua MNDWI. The calibration was carried out by looking for an offset by comparing the averaged MNDWI maps for both sensors throughout the study period. The offset represents the mean bias of the Aqua MNDWI compared with the Terra MNDWI. We added this bias to all daily Terra MNDWI maps to correct for differences between these maps and the corresponding Aqua MNDWI values. This calculation can be expressed as follows:

$$\text{offset} = \overline{\text{MNDWI}}_{\text{Aqua}} - \overline{\text{MNDWI}}_{\text{Terra}} \quad (3)$$

$$\text{MNDWI}_{\text{Terra_cal}} = \text{MNDWI}_{\text{Terra}} + \text{offset} \quad (4)$$

where $\overline{\text{MNDWI}}_{\text{Aqua}}$ and $\overline{\text{MNDWI}}_{\text{Terra}}$ are the averaged MNDWI values throughout the study period from Aqua and Terra, respectively, and $\text{MNDWI}_{\text{Terra_cal}}$ is the daily calibrated MNDWI value from the original Terra MNDWI value ($\text{MNDWI}_{\text{Terra}}$). Then, for each day, we composited the two MNDWI maps (the original Aqua MNDWI map and the calibrated Terra MNDWI map) into a single map: if only one MNDWI value was available for a pixel, we used that value, but if two values were available, we used their average value. This operation increased the temporal resolution of the MNDWI values compared with using MNDWI from a single platform.

Some researchers have utilized AMSR-E data to monitor wetlands by detecting polarization differences [27,28], in particular using the ΔT index:

$$\Delta T = T_{36.5V} - T_{36.5H} \quad (5)$$

where $T_{36.5V}$ and $T_{36.5H}$ represent the brightness temperatures at 36.5 GHz with vertical and horizontal polarization, respectively.

Takeuchi and Gonzalez [12] proposed NDPI as a surface water indicator, based on a normalization of ΔT :

$$\text{NDPI} = \frac{T_{36.5V} - T_{36.5H}}{T_{36.5V} + T_{36.5H}} \quad (6)$$

NDPI describes emissivity differences between the two polarizations when the atmospheric transmission is near to 1, so that it does not depend on the ground temperature [13]. NDPI has greater values in water-covered areas. Many factors affect NDPI, but it should mainly respond to surface water

as well as ΔT does [28]. This is because the difference between the emissivities of the vertical and horizontal polarizations is greater when the ground surface contains more moisture [29]. Theoretically, NDPI takes a value between -1 and 1 , but in practice, it varies within a smaller range: in most cases, it was between 0 and 0.1 in our study area, and it is unlikely to take negative values unless there are materials present that strongly increase the magnetic permeability of the ground, such as ferromagnetics, based on the Fresnel equations [29].

We used two NDPI maps (for ascending and descending orbits) on each day. We calibrated the descending NDPI with the ascending NDPI, and combined the descending NDPI with the ascending NDPI for each day using the same method that we used for MNDWI.

2.4. Database Unmixing

Before we combined the MODIS and AMSR-E/AMSR2 data, we confirmed that MNDWI and NDPI were significantly correlated. The maps of these two indices showed a similar spatial pattern (Figure 4). Although implausibly high NDPI was observed in the Namib Desert along the western coast, probably due to the very smooth surface of the desert [28], we omitted this region from our study because it was obviously unsuitable for rice cultivation. We confirmed a significant correlation (Pearson's r) between MNDWI and NDPI (Figure 5) at sites A, B, and C (Figure 2) for all days during the rainy season. At sites A and B, we found a weaker but still significant correlation (site A, $r = 0.33$, $p < 0.05$; site B, $r = 0.39$, $p < 0.05$), probably due to the combination of relatively small areas of water with the coarse resolution of the satellite data, but we found a strong and significant correlation at site C ($r = 0.86$, $p < 0.05$), where surface water was widely distributed during the rainy season. These results justify our combined use of the MODIS MNDWI and AMSR-E/AMSR2 NDPI values.

Figure 4. Comparison of the spatial patterns of MNDWI and NDPI in the rainy season. Areas with high MNDWI (such as seasonal wetlands, rivers, and the Etosha Pan) have high NDPI and areas with low MNDWI have low NDPI, except for the Namib Desert along the western coast.

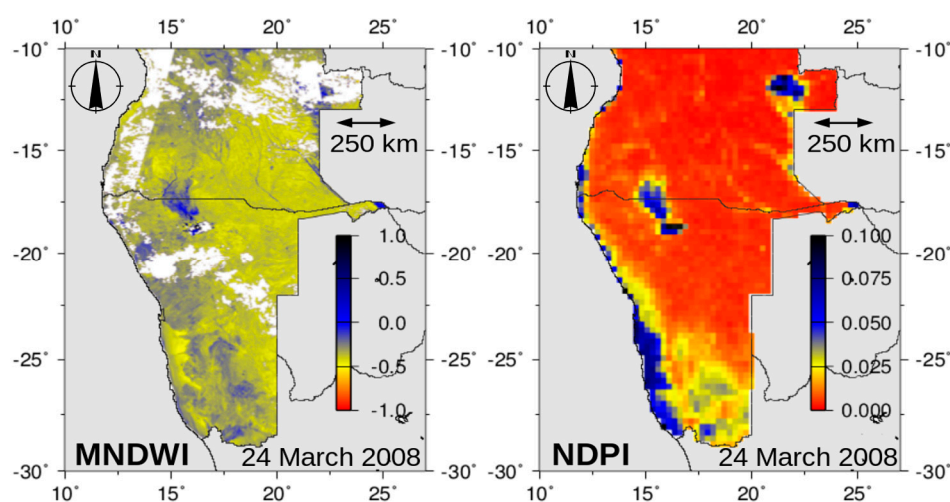


Figure 5. Scatterplots of the correlation between MNDWI and NDPI during the rainy season. (A), (B), and (C) are the test sites defined in Figure 2.

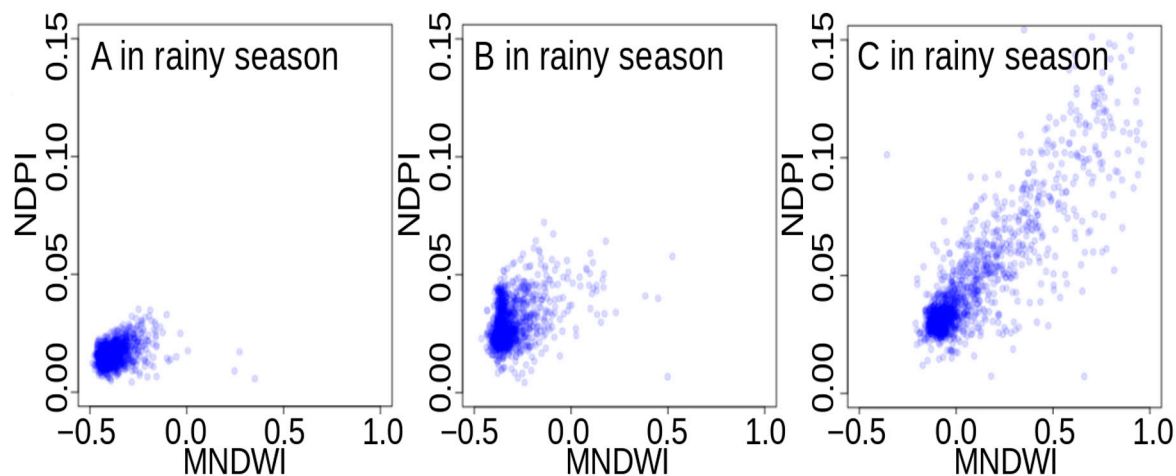
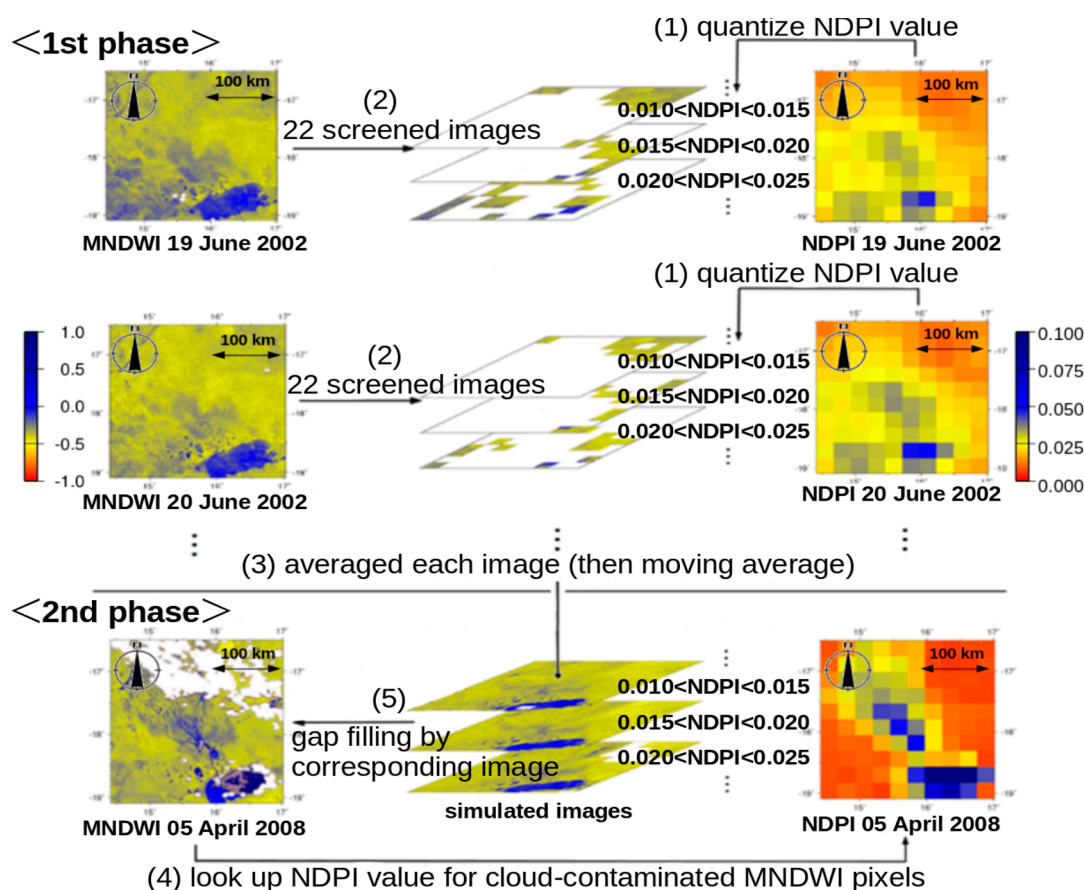


Figure 6 illustrates our “database unmixing” approach. The overall process is a kind of machine learning that consists of two phases: the first phase is learning, and the second phase is prediction.

- In the first phase, we quantized the range of NDPI values into 22 levels, as follows:

level 1:	$\text{NDPI} < 0$
level n ($n = 2, 3, \dots, 21$):	$0.005(n - 2) \leq \text{NDPI} < 0.005(n - 1)$
level 22:	$0.1 \leq \text{NDPI}$

Figure 6. The sequence used for the database unmixing procedure.



Then, for each level, we produced a “screened NDPI image” by keeping the original NDPI pixels if they belonged to the level, and otherwise assigning the pixel a null value. As a result, we obtained 22 NDPI images that corresponded to the 22 levels on each day.

2. Next we produced a “screened MNDWI image” by overlaying the original MNDWI map on each screened NDPI image, and retained only the MNDWI pixels for which the NDPI value was not null, otherwise assigning the pixel a null value. The result was 22 screened MNDWI images that corresponded to the 22 NDPI levels.
3. After completing this operation for all of the maps (*i.e.*, for each day) throughout the study period, we averaged the screened MNDWI images within each level. We then used these 22 averaged MNDWI images to calculate a moving average with two adjacent levels (*i.e.*, the moving window’s size was three), and used these images to represent 22 “simulated MNDWI images”.

We then proceeded to the second phase, in which we used the simulated MNDWI images for gap-filling of the original MNDWI maps to provide values for the missing pixels (due to cloud-contamination or sensor problems) in the original MNDWI map:

4. We examined the NDPI value to identify which NDPI level the missing pixel belonged to.
5. We then replaced the missing pixel with the corresponding value from the simulated MNDWI image that was created based on the NDPI levels.

When both NDPI and MNDWI values were missing, we did not attempt to fill the gap, and assigned a null value to the pixel instead.

This simple approach assumes that the spatial pattern of the wetlands is always the same if the NDPI value is the same. This assumption is approximately valid because the ephemeral wetlands (*oshana*) appear in almost the same place every year. However, the appearance of the wetlands might differ slightly between the wetting stage (when the water surface area increases) and the drying stage (when the water surface area decreases). Therefore, we treated these two stages separately: the wetting stage is from August to January, which includes the beginning of the rainy season (November to January), and the drying stage is from February to July, which includes the end of the rainy season (April). Thus, we obtained 44 simulated MNDWI images (22 images \times 2 stages) and performed the gap-filling separately for each stage.

We validated the gap-filling by comparing the original cloud-free MNDWI map with the fully gap-filled (simulated) MNDWI map. To do so, we selected two cloud-free original MNDWI maps (one from the rainy season and one from the dry season), and started by assigning null values to all of their pixels. We then performed gap-filling using the database unmixing method to create fully gap-filled (simulated) MNDWI maps. We then compared the fully gap-filled (simulated) MNDWI maps with the original cloud-free MNDWI maps, and calculated correlation coefficients between the fully gap-filled maps and the original maps.

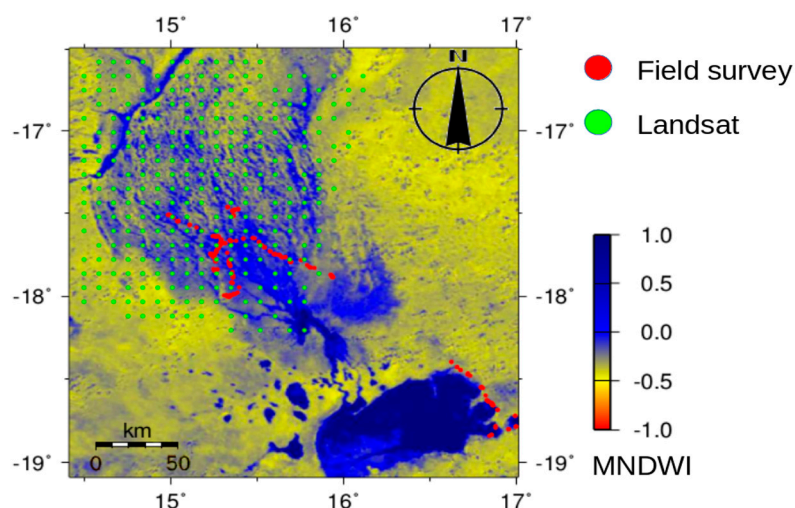
2.5. Receiver-Operator Characteristics Analysis

After performing the gap-filling by means of database unmixing, we applied receiver-operator characteristics (ROC) analysis to the MNDWI maps. ROC analysis is a technique for visualizing and evaluating the performance of a classifier [30], and has been used for pattern recognition in

applications such as remote sensing studies [31]. In our case, we evaluated the performance of MNDWI as a wetland classifier. ROC analysis also provided us with the optimal threshold of MNDWI that could be used to distinguish wetlands from other types of land. We performed this analysis using the R statistical software [32], using the ROC function for R developed by H. Okumura [33], with one modification: we replaced line 22 in the source code of the function (“*th = score_prev*”) by “*th = score[j]*”.

ROC analysis requires reference data that relate MNDWI to the land cover classification. To provide such data, we first related the MNDWI values to ground-truthing data obtained from a field survey and from Landsat Enhanced Thematic Mapper Plus (ETM+) data obtained from USGS EarthExplorer [5]. The field ground-truthing data was prepared using photographs we took with a GPS-equipped camera (EX-H20G, CASIO, Tokyo, Japan) in north-central Namibia. We selected 251 photos, and interpreted the land cover at each location following the scheme of the Site-based dataset for evaluating Annual Change of Land cover types by JAXA (SACLAJ) [34]. We then separated the categories of “water” from all other categories, and defined all other categories as “not water”. As the field survey was mainly performed during the dry season, we could not directly obtain enough ground-truthing data for the rainy season. Instead, we used one scene from the Landsat ETM+ data (path 180, row 072) on a cloudless day during the rainy season (21 March 2009) as a proxy for the ground-truthing data. We divided the scene into a 21×21 grid, and interpreted a pixel as water or not water for each intersection (a total of 20×20 points). If a point occupied a null area in the Landsat data (e.g., due to problems with the scan line corrector), we omitted the point from our analysis. We obtained 281 ground-truthing data from the Landsat scene, for a total of 532 ground-truthing data in the two seasons (Figure 7). We related these ground-truthing data to the MNDWI value on the same day at the same location to obtain reference data for the ROC analysis.

Figure 7. The locations where ground-truthing data were obtained. The ground-truthing data from the field survey were obtained mainly during the dry season, whereas the ground-truthing data from the Landsat data were obtained during a cloud-free day during the rainy season. The background image is the MNDWI distribution derived from the MODIS data (24 March 2008).



ROC analysis evaluated the performance of MNDWI using the area under the ROC curve (AUC). Moreover, we simultaneously determined both the optimal threshold for MNDWI and the error in the recognition of the seasonal wetlands and dry land using the jack-knife method, which is a basic method for cross-validation: we picked 531 of the 532 reference data points provided by the ground-truthing to determine the threshold that minimized the balanced error rate (BER) for the land classification using the ROC function. We then tested whether the threshold correctly classified a pixel using the one remaining reference data point. We repeated this operation for each of the reference data (*i.e.*, a total of 532 times) using a Linux shell script. We determined the optimal threshold as the average of all the computed thresholds, and determined the error under the optimal threshold as the overall rate of mis-classification.

2.6. Extraction of the Area Potentially Suitable for Rice Cultivation

After defining the threshold MNDWI from the ROC analysis, we extracted the water-covered area on each day. We calculated the probability of water presence (PWP) both in the rainy season (November to April) and for the whole year, for each year and for the study period as a whole. We defined PWP as the number of days in which the water covered a given location divided by the number of days for which image data was available (*i.e.*, excluding null pixels). We assumed that the area potentially suitable for rice cultivation included locations where PWP during the rainy season was greater than 41.7% (*i.e.*, for 2.5 out of 6 months), except for permanent wetlands (e.g., ponds, lakes, rivers) in which the PWP for the whole year was greater than 50% (*i.e.*, for 6 out of 12 months). This is because the fastest-growing NERICA (New Rice for Africa) cultivar takes about 75 days (2.5 months) to reach maturity [35].

3. Results

Figure 8 illustrates an example of gap-filling of the MNDWI maps. The characteristic patterns such as rivers and lakes were reproduced well by the database unmixing. However, in some seasonal wetlands and some dry land (the red circles in Figure 8), an implausible pattern was observed. For example, the circle at site A encloses an area with implausibly high MNDWI, which is unlikely to exist because this site is an area of dry land with arenosols, which drain rapidly. By examining the left figure (before gap-filling), this unreasonably high MNDWI appears to have resulted from cloud contamination that was not eliminated during preprocessing, rather than from an error in the database unmixing. On the other hand, the circle at site B, which is part of the *oshana* network, does not show a pattern of high MNDWI, which suggests an error in the database unmixing procedure.

Figure 9 provides a qualitative validation of the database unmixing method. In the dry land, database unmixing tended to simulate MNDWI values lower than the original value (e.g., in the red circle). On the other hand, in water-covered areas such as rivers and the Etosha Pan, the simulated MNDWI tended to be larger than the original value (e.g., in the blue circle). The correlation coefficient (Pearson's r) between the fully gap-filled map and the original map from the rainy season (24 March 2008) was 0.89 ($p < 0.05$), and that from the dry season (30 September 2008) was 0.86 ($p < 0.05$).

Figure 8. The result of gap-filling using the database unmixing method. The left figure is the map before gap-filling and the right is the map after gap-filling. The red circles represent an implausibly high MNDWI at site A and a too-low MNDWI at site B.

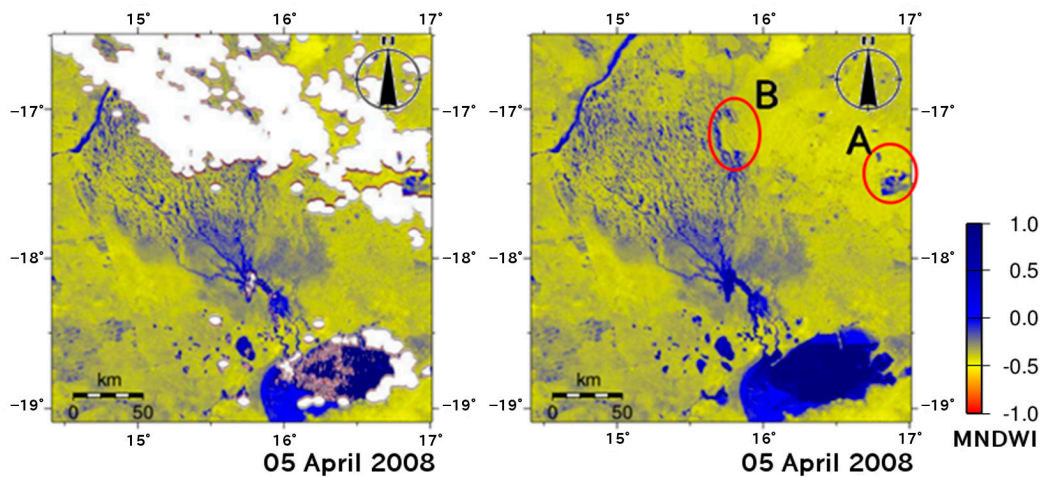
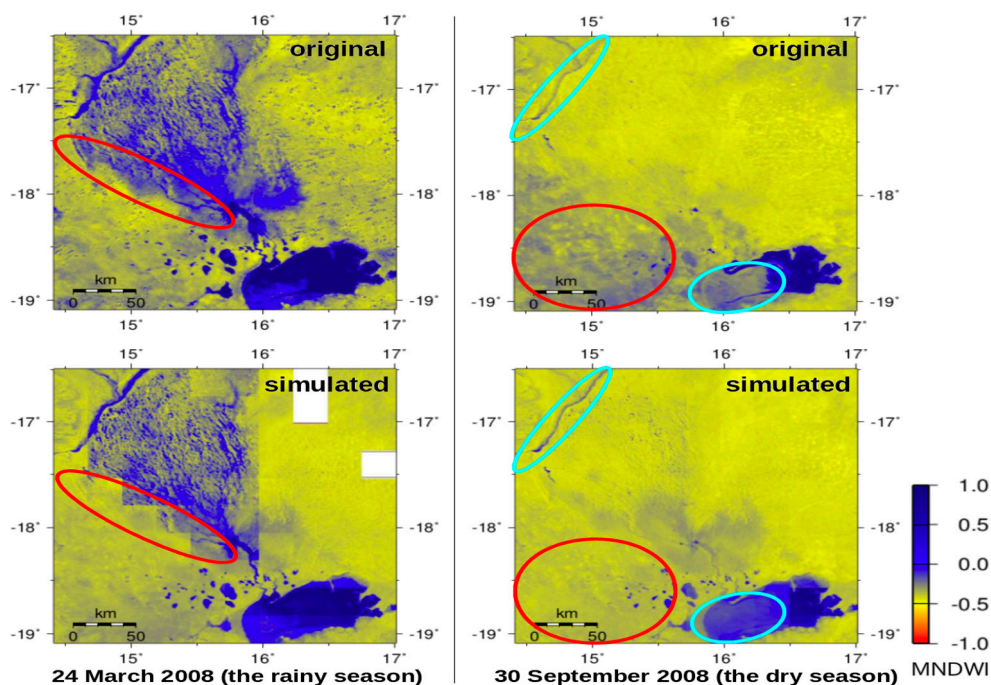


Figure 9. Comparison between (top) the original MNDWI maps and (bottom) the fully gap-filled (simulated) MNDWI maps for two days. During the rainy season (24 March 2008) there were some failures (null pixels) in the gap-filling. The red circles represent areas with MNDWI values lower than the original value; the blue circles represent areas with MNDWI greater than the original value.



By combining the MODIS and AMSR-E/AMSR2 data using the database unmixing procedure, we increased the total amount of MNDWI data that was available (from 73% of pixels to an average of 91%). In particular, the amount of MNDWI data during the rainy season improved dramatically: from 53% of pixels to an average of 80% during the whole rainy season, and from 36% to an average of 81% in the middle of the rainy season (January).

Through the ROC analysis, we estimated that $AUC = 0.747$, the threshold $MNDWI = -0.316$, and the error in the recognition of seasonal wetlands and dry lands was 21.2%.

Figures 10 and 11 show the probability of water presence (PWP) during the rainy season (November to April) and the precipitation in each month from 2005 to 2011. We used correlation analysis to confirm that the PWP maps were related to precipitation during the rainy season; that is, high precipitation caused high PWP during the rainy season. The mean value in the PWP map for each rainy season was strongly and significantly correlated with the total precipitation during each rainy season ($r = 0.837$, $p < 0.05$). The areas with high PWP therefore appear to represent seasonal wetlands.

Figure 10. Probability of water presence (PWP) and precipitation during the rainy season from 2005 to 2008. Precipitation data were from Mendelsohn *et al.* [36].

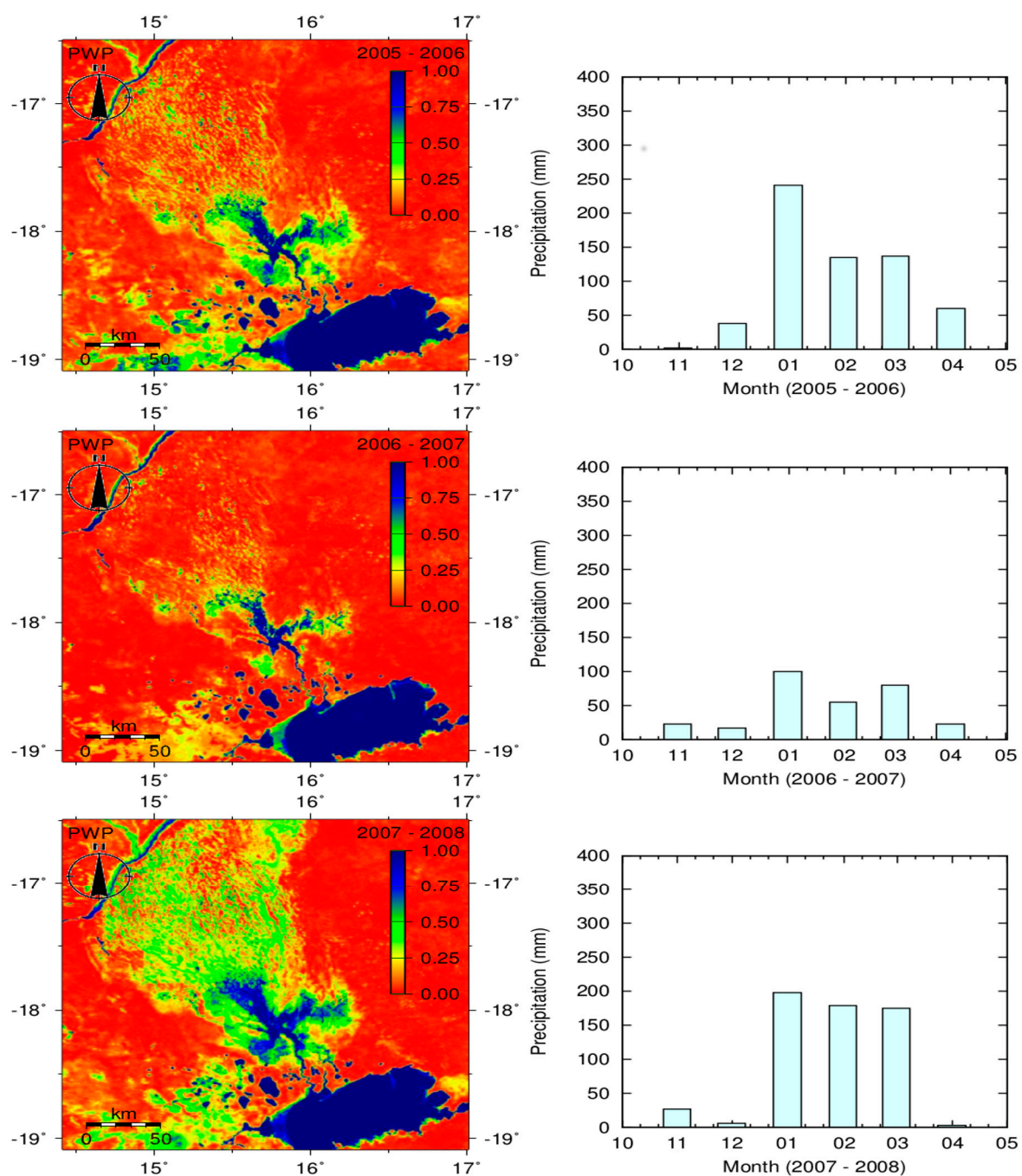
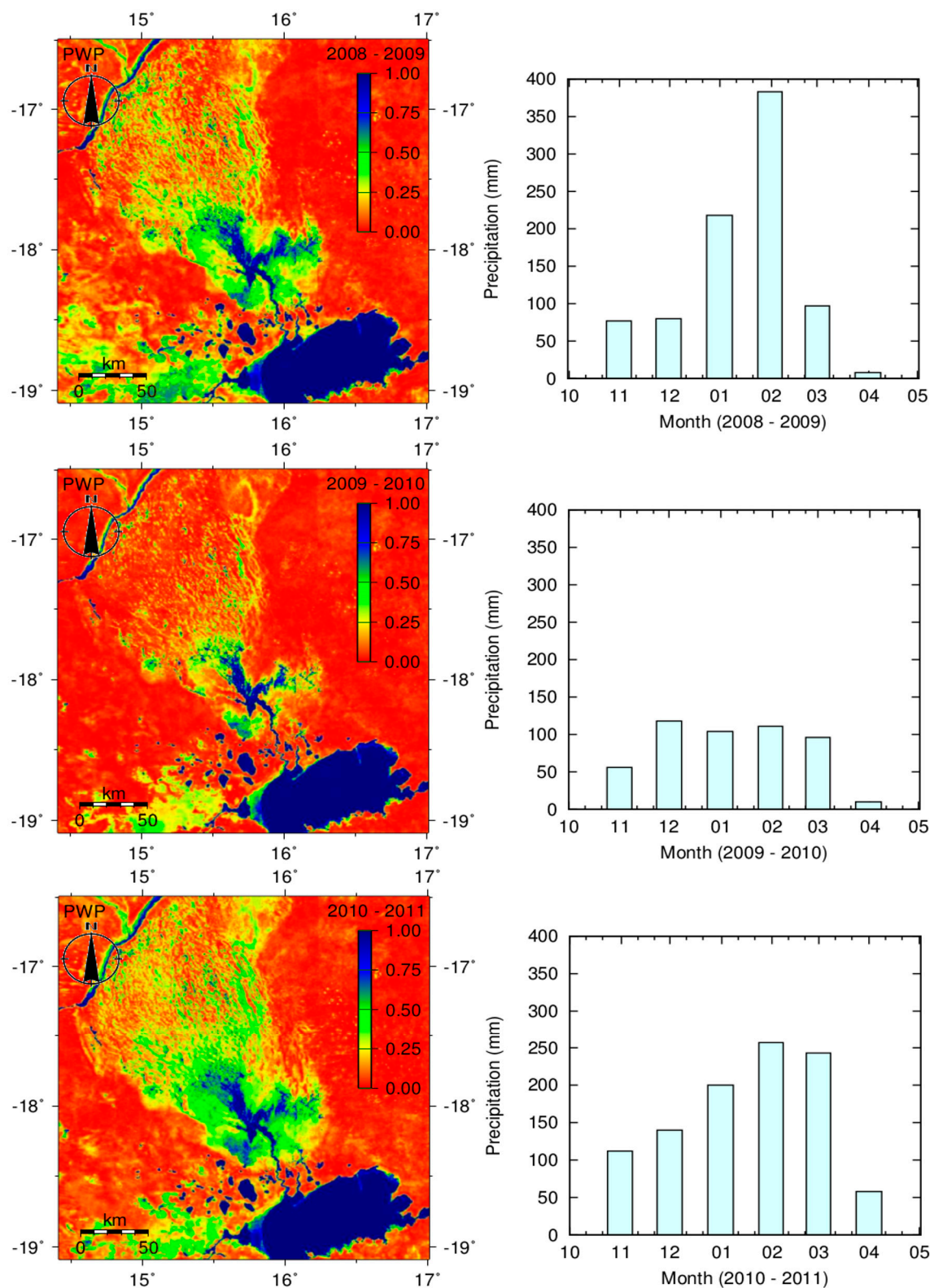


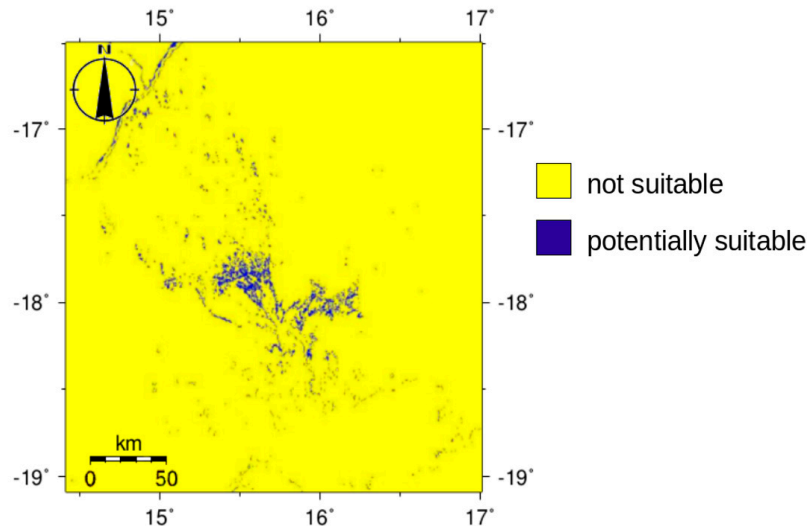
Figure 11. Probability of water presence (PWP) and precipitation during the rainy season from 2008 to 2011. Precipitation data were from Mendelsohn *et al.* [36].



Finally, we identified the area that was potentially suitable for rice cultivation: this represented the area for which PWP was greater than 41.7% during the rainy season, but excluding permanent wetlands. This totaled 1255 km² (1.6% of our study area). The potentially suitable area was mainly distributed in

the seasonal wetlands, but some was distributed along the Kunene River and at the edges of the Etosha Pan (Figure 12).

Figure 12. The distribution of the areas potentially suitable for rice cultivation.



4. Discussion

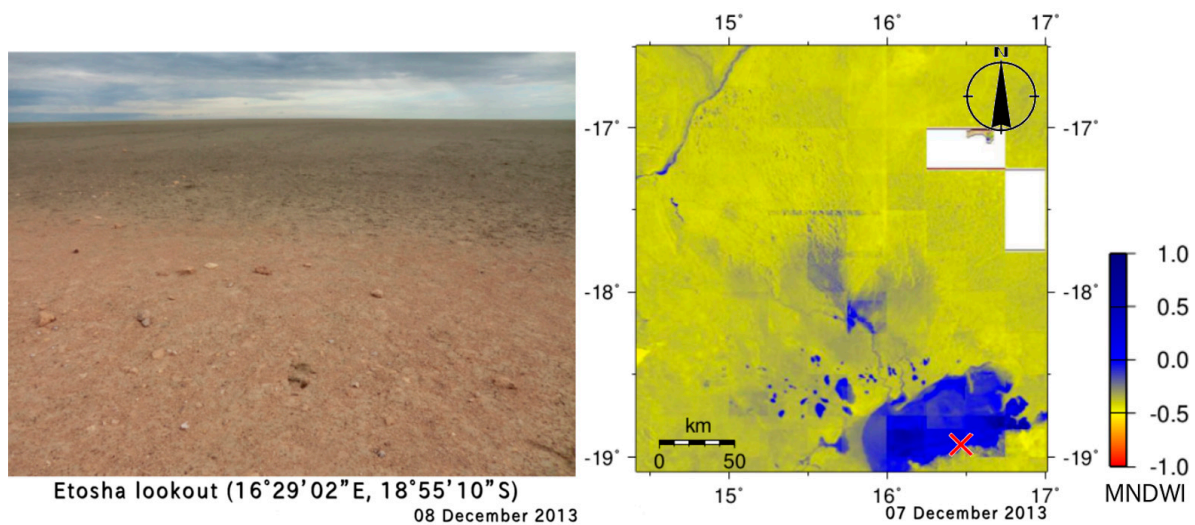
The database unmixing provided daily MNDWI maps with higher temporal resolution than the original maps. In other words, we generated weather-independent, MODIS-resolution maps. These data became the basic information that we used for hydrological analysis to accurately evaluate the distribution of surface water, especially during the rainy season. This let us estimate the area potentially suitable for rice cultivation, which provides a good starting point for additional analysis of the feasibility of rice introduction. The large improvement in the overall availability of MNDWI data for the study area suggests that this gap-filling method can be applied in other cases where cloud contamination would make it difficult to use MODIS MNDWI data, such as in tropical rain forests.

Because AUC was greater than 0.7, MNDWI was able to distinguish seasonal wetlands and dry land with moderately good performance [37]. The error rate for the recognition of the two types of land was moderately low, with an error of 21.2%. Our validation of the gap-filling procedure showed that the predictions produced by the database unmixing were reliable ($r = 0.89$ for the rainy season, $r = 0.86$ for the dry season), but it also suggests that the database unmixing tends to exaggerate MNDWI: the dry lands were estimated as being drier (lower MNDWI), and the wetlands were estimated as being wetter (higher MNDWI). These results suggest that there is still room for improvement in the algorithm and in the reference data. In particular, it may be possible to identify a better indicator than MNDWI, find a dataset with more reference data, or perform more accurate cloud and cloud-shadow screening. However, there is likely to be a trade-off between the accuracy of cloud screening and the accuracy of database unmixing because excessive screening decreases the amount of original data available for database unmixing. The NDPI quantization level in the database unmixing should also be considered, but there is also a trade-off: excessive division of NDPI into levels decreases the amount of original data available for any given level of NDPI, whereas dividing NDPI into too few levels decreases the ability to adequately describe the levels of NDPI. In addition, the

process of separating the data into two environmental stages (the drying and wetting stages) in the database unmixing should be refined to confirm that these are the optimal stages.

As Figures 10 and 11 illustrate, the size of the area with high PWP varies dramatically from year to year. The size of the area with high PWP was positively correlated with the amount of precipitation. However, in some regions such as the Etosha Pan and the arenosol area west of Etosha, PWP seems to be too high. In fact, field surveys suggest that the water does not always accumulate in the Etosha Pan during the rainy season. We took photos in the Etosha Pan on 8 December, 2013, and confirmed that there was little water, except for a small pool created by local rain. However, the nearest day's MNDWI map (Figure 13) showed high MNDWI, as if there was significant water present. This misrecognition may be due to the smooth surface and high soil moisture content in the Etosha Pan. Where the ground surface has particular characteristics such as these ones, it might be difficult to use NDPI and MNDWI to distinguish surface water from very moist soil. This result shows the limitations of using NDPI and MNDWI; thus, improving these water indices will be an important issue in future research.

Figure 13. Photograph taken at the Etosha lookout (the red x) and the gap-filled MNDWI map for the closest day. We could not obtain a gap-filled MNDWI map for the same day when the photo was taken because no NDPI map was available for database unmixing.



The calculated area that is potentially suitable for rice cultivation will require careful discussion from the perspectives of soil conditions (e.g., soil type, water permeability, salinity), topography, geographical or sociological factors (e.g., accessibility for farmers, ownership of the field, water rights), the influence on the water budget, and so on. In particular, water depth and duration in the wetlands is one of the biggest issues that would affect actual rice cultivation. The water duration has been accounted for by using short-span PWP analysis (*i.e.*, PWP screening during the rainy season to define potentially suitable areas). The water depth, however, has not yet been determined, and both factors are important. This could be analyzed by using high-resolution satellite images combined with a digital elevation model (DEM); however, the existing DEMs available from satellite measurements such as GTOPO30 and the Advanced Spaceborne Thermal Emission and Reflection Radiometer Global Digital Elevation Model (ASTER GDEM) do not provide enough spatial resolution (in both the horizontal and

the vertical directions). Field measurements based on laser scanning [38] or obtained by using an unmanned aerial vehicle [39,40] may be a promising solution. In addition, our results should be field-validated and compared with other surface water maps (e.g., provided by NASA [41]) to detect any problems with our method.

Despite the abovementioned issues, satellite remote sensing allowed us to create a relatively high-resolution PWP map. From a practical perspective, farmers utilize smaller-scale isolated seasonal wetlands (at most, 100 m in resolution) that would not be detected at the MODIS image resolution. It will therefore be necessary to try different combinations of data, such as combining MODIS with the Phased Array type L-band Synthetic Aperture Radar (PALSAR) or Landsat data, to develop PWP maps with higher resolution by means of database unmixing.

Despite the coarse resolution of the MODIS data, our approach offers an important possible application: it allows researchers to quickly identify the parts of our study area (*i.e.*, those with a sufficiently high PWP) that deserve more attention from field surveys to confirm their suitability. With appropriate sensor data, the database unmixing approach will provide maps with higher spatial and temporal resolution that would enable more accurate analysis and better agricultural planning.

5. Conclusions

In this paper we evaluated the surface water distribution in north-central Namibia to estimate the area potentially suitable for rice cultivation by using data from two different types of sensors: the MODerate-resolution Imaging Spectroradiometer (MODIS) and the Advanced Microwave Scanning Radiometer (AMSR) series. First, we introduced two water indices: the modified normalized-difference water index (MNDWI) and the normalized-difference polarization index (NDPI). Then we developed a simple matching method that we named “database unmixing” to fill gaps in the data created by cloud and cloud-shadow contamination of the MNDWI maps. The database unmixing assumes that the spatial pattern of the wetlands (*i.e.*, the spatial pattern of surface water and of moist and smooth surfaces) remains constant if the NDPI value does not change. The database unmixing increased the available MNDWI data (from 73% of pixels to an average of 91% during the whole year, and from 53% of pixels to an average of 80% during the rainy season), which enabled us to produce weather-independent, MODIS-resolution maps. From the gap-filled MNDWI maps, we extracted the wetland areas by using a threshold MNDWI ($\text{MNDWI} = -0.316$) based on receiver-operator characteristics (ROC) analysis, and found a moderately low mis-classification error (21.2%). MNDWI performed moderately well as a classifier of water pixels *versus* not-water pixels based on the area under the ROC curve (AUC), which was 0.747.

To describe the surface water distribution in the wetlands, we aggregated the extracted water presence maps into probability of water presence (PWP) maps for the rainy season and the whole year, and estimated the area potentially suitable for rice cultivation. The total area potentially suitable for rice cultivation was 1255 km² (1.6% of the study area); we have used this data to create the first map that provides a good starting point for a more focused analysis of the feasibility of rice introduction in the study area. Although this provides a good preliminary estimate, it will be necessary to confirm that the water depth is also suitable. Database unmixing should be refined from the perspectives of the two indices that we used (MNDWI and NDPI) and of each element of the algorithm (e.g., cloud and

cloud-shadow screening, quantization levels, separate treatment of the drying and wetting stages), and should be compared with field reference data and with other approaches such as classification trees and neural networks to provide more rigorous validation. Database unmixing will be useful for other areas and other satellite datasets that are affected by cloud cover during all or specific parts of the year. This approach provides maps with higher spatial and temporal resolution; therefore, it can support many additional types of remote-sensing analysis.

Acknowledgments

This research was supported by JST/JICA, the Science and Technology Research Partnership for Sustainable Development (SATREPS), and JAXA's Global Change Observation Mission (GCOM: PI#102). We also thank Morio Iijima and Yuichiro Fujioka (Kinki University) and Jack R. Kambatuku, Johanna N. Niipele, and all members of the Faculty of Agriculture and Natural Resources, University of Namibia (UNAM) for their support during our field survey.

Author Contributions

Hiroki Mizuochi built the research design from the aspect of remote sensing, implemented all the analysis (including development of the water index, applying database unmixing, collection of field data and validation of the algorithm), and wrote this manuscript. Tetsuya Hiyama and Takeshi Ohta built the research design from the hydrological aspect, and supported the field survey and the manuscript writing. Kenlo Nishida Nasahara built the research design from the aspect of remote sensing including the basic concept of database unmixing, and supported the manuscript writing.

Conflicts of Interest

The authors declare no conflict of interest.

References

1. Mendelsohn, J.; Jarvis, A.; Roberts, C.; Robertson, T. The land. In *Atlas of Namibia—A Portrait of the Land and Its People*; David Philip Publishers: Cape Town, South Africa, 2002; p. 152.
2. Bethune, S.; Amakali, M.; Roberts, K. Review of Namibian legislation and policies pertinent to environmental flows. *Phys. Chem. Earth.* **2005**, *30*, 894–902.
3. Mendelsohn, J.; Obeid, E.S.; Roberts, C. Farming. In *A Profile of North-Central Namibia*; Gamsberg Macmillan Publishers: Windhoek, Namibia, 2000; p. 51.
4. Mendelsohn, J.; Jarvis, A.; Robertson, T. An introduction. In *A Profile and Atlas of the Cuvelai-Etoshia Basin*; John Meinert Printing Windhoek: Windhoek, Namibia, 2013; pp. 9–14.
5. USGS EarthExplorer. Available online: <http://earthexplorer.usgs.gov> (accessed on 4 June 2014).
6. Suzuki, T.; Ohta, T.; Hiyama, T.; Izumi, Y.; Mwandemele, O.; Iijima, M. Effects of the introduction of rice on evapotranspiration in seasonal wetlands. *Hydrol. Proces.* **2013**, *28*, doi:10.1002/hyp.9970.

7. Hiyama, T.; Suzuki, T.; Hanamura, M.; Mizuochi, H.; Kambatuku, J.R.; Niipele, J.N.; Fujioka, Y.; Ohta, T.; Iijima, M. Evaluation of Surface Water Dynamics for Water-Food Security in Seasonal Wetlands, North-Central Namibia. Available online: http://iahs.info/uploads/dms/1_16531.Abstracts-for-web-site-63.pdf (accessed on 31 March 2014).
8. Iijima, M.; Awala, K.S.; Mwandemele, D.O. Introduction of subsistence rice cropping system harmonized with the water environment and human activities in seasonal wetlands in northern Namibia. In Proceedings of the Science and Technology Research Partnership for Sustainable Development (SATREPS) Rice-Mahangu Project International Symposium, Nagoya, Japan, 13 July 2013.
9. SATREPS Research Project. Flood- and Drought- Adaptive Cropping Systems to Conserve Water Environments in Semi-Arid Regions. Available online: http://www.jst.go.jp/global/english/kadai/h2306_namibia.html (accessed on 16 July 2014).
10. Suzuki, T.; Ohta, T.; Izumi, Y.; Kanyomeka, L.; Mwandemele, O. Role of canopy coverage in water use efficiency of lowland rice in early growth period in semi-arid region. *Plant Prod. Sci.* **2013**, *16*, 12–23.
11. Mendelsohn, J.; Obeid, E.S.; Roberts, C. Water. In *A Profile of North-Central Namibia*; Gamsberg Macmillan Publishers: Windhoek, Namibia, 2000; p. 16.
12. Takeuchi, W.; Gonzalez, L. Blending MODIS and AMSR-E to predict daily land surface water coverage. In Proceedings of the International Remote Sensing Symposium (ISRS), Busan, Korea, 29 October 2009.
13. Zheng, W.; Liu, C.; Xin, Z.; Wang, Z. Flood and waterlogging monitoring over Huaihe River Basin by AMSR-E data analysis. *Chin. Geogra. Sci.* **2008**, *18*, 262–267.
14. Dasgupta, S.; Qu, J.J. Combining MODIS and AMSR-E based vegetation moisture retrievals for improved fire risk monitoring. In Proceedings of the Remote Sensing and Modeling of Ecosystems for Sustainability III, San Diego, CA, USA, 13 August 2006.
15. Gamon, A.; Serrano, L.; Surfus, S. The photochemical reflectance index: An optical indicator of photosynthetic radiation use efficiency across species, functional types, and nutrient levels. *Oecologia* **1997**, *112*, 492–501.
16. NASA LP DAAC Data Pool. Available online: <http://e4ftl01.cr.usgs.gov> (accessed on 24 February 2014).
17. NASA DAAC at NSIDC Data Pool. Available online: ftp://n5eil01u.ecs.nsidc.org/SAN/AMSA/AE_Land3.002 (accessed on 24 February 2014).
18. JAXA GCOM-W1 Data Providing Service. Available online: <https://gcom-w1.jaxa.jp/auth.html> (accessed on 24 February 2014).
19. NASA DAAC at NSIDC, MODIS Data. Available online: http://nsidc.org/data/modis/terra_aqua_differences (accessed on 10 June 2014).
20. GRASS GIS. Available online: <http://grass.osgeo.org/> (accessed on 8 August 2014).
21. Takeuchi, W.; Yasuoka, Y. Development of normalized vegetation, soil and water indices derived from satellite remote sensing data. *J. Jpn Soc. Photogramm. Remote Sens.* **2004**, *43*, 7–19. (In Japanese)
22. McFeeters, S.K. The use of the Normalized Difference Water Index (NDWI) in the delineation of open water features. *Int. J. Remote Sens.* **1996**, *17*, 1425–1432.

23. Xu, H. Modification of normalised difference water index (NDWI) to enhance open water features in remotely sensed imagery. *Int. J. Remote Sens.* **2006**, *27*, 3025–3033.
24. Gao, B. NDWI—A Normalized Difference Water Index for remote sensing of vegetation liquid water from space. *Remote Sens. Environ.* **1996**, *58*, 257–266.
25. Murai, S. Remote sensing note. In *Japan Association of Remote Sensing*; NASA: Washington, DC, USA 1992; p. 19. Available online: www.jars1974.net/pdf/rsnote_e.html (accessed on 23 February 2014).
26. Google Map Panoramio. Available online: <http://www.panoramio.com/map> (accessed on 7 June 2014).
27. Choudhury, B.J. Passive microwave remote sensing contribution to hydrological variables. *Surv. Geophys.* **1991**, *12*, 63–84.
28. Sippel, S.J.; Hamilton, S.K.; Melack, J.M.; Choudhury, B.J. Determination of inundation area in the Amazon River floodplain using the SMMR 37 GHz polarization difference. *Remote Sens. Environ.* **1994**, *76*, 70–76.
29. Ulaby, F.T.; Moore, R.K.; Fung, A.K. Radiometry. In *Microwave Remote Sensing*; Addison-Wesley Publishing Company: Reading, MA, USA, 1981; Volume 1, pp. 230–231.
30. Fawcett, T. An introduction to ROC analysis. *Pattern Recogn. Lett.* **2006**, *27*, 861–874.
31. Alatorre, L.C.; Sánchez-Andrés, R.; Cirujano, S.; Beguería, S.; Sánchez-Carrillo, S. Identification of mangrove areas by remote sensing: The ROC curve technique applied to the northwestern Mexico coastal zone using Landsat imagery. *Remote Sens.* **2011**, *3*, 1568–1583.
32. The R Project for Statistical Computing. Available online: <http://www.r-project.org/> (accessed on 8 August 2014).
33. Statistics and Data Analysis. Available online: <http://oku.edu.mie-u.ac.jp/~okumura/stat/ROC.html> (accessed on 23 February 2014).
34. SACLAIJ. Available online: <http://pen.agbi.tsukuba.ac.jp/~lulc/hiki/?SACLAIJ> (accessed on 23 February 2014).
35. Jones, M.P.; Mande, S.; Aluko, K. Diversity and potential of *Oryza glaberrima* steud in upland rice breeding. *Breeding Sci.* **1997**, *47*, 395–398.
36. Mendelsohn, J.; Jarvis, A.; Robertson, T. Climate. In *A Profile and Atlas of the Cuvelai-Etosha Basin*; John Meinert Printing Windhoek: Windhoek, Namibia, 2013; p. 45.
37. Antognoli, M.C.; Remmenga, M.D.; Bengtson, S.D.; Clark, H.J.; Orloski, K. A; Gustafson, L.L.; Scott, A.E. Analysis of the diagnostic accuracy of the gamma interferon assay for detection of bovine tuberculosis in U.S. herds. *Prev. Vet. Med.* **2011**, *101*, 35–41.
38. Hayakawa, Y.S.; Kontani, R.; Ezer, S.; Ozturk, G. *A Quasi Laser Scanning System Using Laser Range Finder and Automatic Panorama Shooting Device*; Center for Spatial Information Science (CSIS): Tokyo, Japan, 2012.
39. James, M.R.; Robson, S. Straightforward reconstruction of 3D surfaces and topography with a camera: Accuracy and geoscience application. *J. Geophys. Res.* **2012**, *117*, doi:10.1029/2011JF002289.
40. Rosnell, T.; Honkavaara, E. Point cloud generation from aerial image data acquired by a quadrocopter type micro unmanned aerial vehicle and a digital still camera. *Sensors* **2012**, *12*, 453–480.

41. Near Real-Time Global MODIS Flood Mapping, NASA Goddard and Dartmouth Flood Observatory. Available online: <http://oas.gsfc.nasa.gov/floodmap> (accessed on 8 July 2014).

© 2014 by the authors; licensee MDPI, Basel, Switzerland. This article is an open access article distributed under the terms and conditions of the Creative Commons Attribution license (<http://creativecommons.org/licenses/by/3.0/>).